

Article

Influence of Silicon and Chromium on the Na₂SO₄-Induced Hot Corrosion Behavior of Titanium Alloys

Marzena Mitoraj-Królikowska 

Inorganic Chemistry Department, Faculty of Materials Science and Ceramics, AGH University of Krakow, Al. Mickiewicza 30, 30-059 Krakow, Poland; mmitoraj@agh.edu.pl

Abstract: Titanium alloys are widely used as construction materials in the aerospace and automotive industries. They have many advantages but also have limitations related to their susceptibility to high-temperature oxidation and hot corrosion. Many efforts to increase the lifetime of components made of titanium alloys have been reported in the literature; the most promising ones involve the deposition of coatings. The present paper is focused on the development of coatings containing chromium and silicon, and their further evaluation in hot corrosion tests. It was proved that the Cr-Si coatings were more effective than Si coatings alone in protecting the titanium alloys against Na₂SO₄-induced hot corrosion at 800 °C. The enhanced corrosion resistance was attributed to the preferential formation of a thick and continuous SiO₂ layer on the surface and—in the case of titanium aluminide alloy—the growth of an Al₂O₃-rich inner layer of the scale, promoted by chromium.

Keywords: Na₂SO₄-induced hot corrosion; Cr-Si coatings; titanium alloys



Citation: Mitoraj-Królikowska, M. Influence of Silicon and Chromium on the Na₂SO₄-Induced Hot Corrosion Behavior of Titanium Alloys. *Crystals* **2023**, *13*, 948. <https://doi.org/10.3390/cryst13060948>

Academic Editor:
Petros Koutsoukos

Received: 15 May 2023
Revised: 3 June 2023
Accepted: 8 June 2023
Published: 12 June 2023

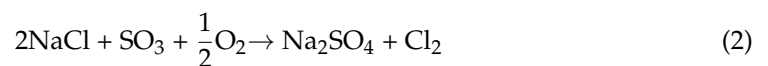
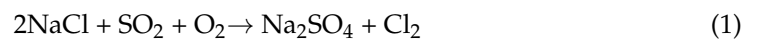


Copyright: © 2023 by the author. Licensee MDPI, Basel, Switzerland. This article is an open access article distributed under the terms and conditions of the Creative Commons Attribution (CC BY) license (<https://creativecommons.org/licenses/by/4.0/>).

1. Introduction

Titanium alloys are widely used as construction materials due to their favorable combination of low density (about 50% lower than steel), high strength, and good resistance to wear and oxidation. Titanium and its alloys also have very good chemical stability and are resistant to many aggressive environments, such as diluted sulfuric and hydrochloric acids, chloride solutions, and most organic acids, which make them interesting materials for the marine and biotechnology industries [1]. Depending on the specific application, different types of titanium alloys are considered. The main categories are based on the alloy phase composition; therefore, α , near- α , $\alpha + \beta$, and β titanium alloys can be recognized. α -alloys, as a commercially pure (CP) material, grades 1–4, or Ti-Pd alloys are commonly used for airplane parts, cryogenic applications, and chemical processing equipment. Near- α alloys mainly contain α -stabilizers with a smaller quantity of β -stabilizing elements (<2 wt%). The microstructure of the near- α alloys consists of a small-volume fraction of hard β -Ti dispersed between a much larger-volume fraction of α -Ti grains. Examples such as Ti-5Al-2Mn, Ti-3Al-2.5V, Ti-5Al-1Sn-1Zr-1V, or Ti-5.8Al-4Sn-3.5Zr-0.7Nb-0.5Mo-0.35Si-0.06C can be mentioned. Near- α alloys are used more often than α -alloys in aircraft, because of their better high-temperature properties, in particular strength and creep resistance. $\alpha + \beta$ dual-phase titanium alloys containing 4–6 wt% of β stabilizers exhibit a variety of microstructures and mechanical properties [2,3]. Ti-6Al-4V [wt%], representing this group of alloys, is the most popular titanium alloy due to its unique balance of mechanical and corrosion properties, which can also be optimized using heat treatments. In the aerospace industry, Ti-6Al-4V is a constructional material; for example, it is used for airframes, and it is used as a component of engines, e.g., compressor blades [4–6]. Its biocompatibility makes this alloy also useful for biomedical applications [7,8], such as knee and hip joints [9,10] and dental implants [11]. It is also present in the marine industry [12,13]; however, it could suffer from oxidative erosion and degradation reactions that affect its resistance to corrosion during exposure to the marine environment [14]. In the context of high-temperature applications, titanium alloys are often used in the aerospace [15] and automotive [16] industries

despite initially being a higher investment compared to other materials. However, clear economic benefits can be seen in the final application, when considering the long-term performance of device components. Today, different titanium alloys are used in high-pressure compressors [17], aircraft turbine engines [18], landing gears [19], low-pressure-turbine (LPT) air foils in General Electric engines [20], and hundreds of minor elements, e.g., door counterbalance clock springs [15]. It is obvious that in these specific applications, materials are exposed to severe working conditions and therefore the requirements for them are relatively high. The main problems related to titanium alloys are susceptibility to oxidation and hot corrosion [21,22]. In particular, hot corrosion can cause fast material deterioration and increase economic costs. This accelerated corrosion is caused by salt deposits at high temperatures under oxidizing conditions [23]. Common salt deposits are NaCl and Na₂SO₄, in which Na₂SO₄ is the main chemical compound related to fuel combustion [24]. Fuels contain sulfur (commercial aviation fuel contains 400–800 ppm of sulfur [25]), which, in oxidizing environments and in the presence of alkali metal impurities, can form sodium sulfate deposits [26]. Na₂SO₄ can be also a product of NaCl (from seawater environments) and SO₂ from fuel combustion according to the following reactions [27]:



Different attempts have been made to reduce the negative influence of salt deposits on titanium corrosion behavior and increase the lifetime of components. Until now, the predominant and the most effective method has been the deposition of coatings. In the literature, depending on the final application and corrosion conditions, a large number of coating compositions and processes can be found [28–30]. For example, coatings have been obtained using thermal spraying [31], sol-gel [32,33], and different types of PVD or CVD techniques [34–36].

For high-temperature oxidation, the main components of coatings are well-known protective oxides such as Al₂O₃, Cr₂O₃, or SiO₂. Among the recently reported ones dedicated to high-temperature protection, the following seem to be worth mentioning. A SiO₂ coating on a γ -TiAl alloy (Ti-50 at% Al) obtained with electrodeposition improved hot corrosion resistance in the presence of a 75wt% Na₂SO₄ + 25wt% NaCl mixed salt deposit for 100 h at 700 °C [37]. The protective properties of the SiO₂ coating were related to the composition of the scale comprising an amorphous SiO₂ with embedded crystals of cristobalite and Na₂Si₄O₉. SiO₂ was also the main component of an enamel coating [38] deposited on Ti-46Al-2Cr-2Mo (at%) which effectively protected an alloy contaminated with 85 wt% Na₂SO₄ and 15 wt% NaCl against oxidation in air at 850 °C for 1, 5, 10, 25, and 50 h. A combination of aluminizing, anodization, and preoxidation was used to improve the hot corrosion resistance of a Ti-50Al (at%) alloy in a mixture of salts consisting of 75 wt% Na₂SO₄ and 25 wt% NaCl at 700 °C [39]. The gradient coating achieved through this combination of methods was promising for corrosion protection, but it was also beneficial for internal stress reduction. The pack cementation method was used to successfully deposit a Si-Al-Y coating on a Ti-48Al-2Cr-2Nb (at%) alloy; however, it had limited-time protective properties in a 25wt% K₂SO₄ + 75wt% Na₂SO₄ corrosive environment at 900 °C [40]. Silicide diffusion coatings were also used for Ti-46Al-8Ta (at%) alloy protection against hot corrosion caused by NaCl or/and Na₂SO₄ salt deposits [41]. The effectiveness of the protection was related to the SiO₂ layer formed during a hot corrosion test. TiN and TiAlN coatings were deposited using arc ion plating on titanium alloys to study their hot corrosion resistance when they were exposed to NaCl at 600 °C [42]. A 12 μm thick TiN coating showed poor corrosion resistance due to its porous and nonprotective oxide scale, whereas for a TiAlN coating produced in a corrosive environment, an Al₂O₃ scale acted as a barrier retarding the inward transport of corrosive species. However, a thicker coating was recommended by the authors.

The aim of this work was to obtain a multicomponent coating containing chromium and silicon as crystalline Cr-Si and Ti-Si phases and to experimentally prove that synergistic Cr and Si protection is more effective for different types of titanium alloys in Na₂SO₄-induced hot corrosion conditions. This work is a continuation of some preliminary studies [43] that indicated the good resistance of Cr-Si coatings to oxidation and hot corrosion caused by NaCl deposits.

2. Materials and Methods

The investigated titanium alloys had different compositions and microstructures. Their chemical compositions are collected in Table 1, whereas microstructures are shown in Figure 1. The pseudo α (also called near α) Ti-5Al-2Mn (at%) (OT4-1) and ($\alpha + \beta$) Ti-11Al-2.5Mo-2.5Cr (at%) (VT3-1) were commercially available, while ($\gamma + \alpha_2$) Ti-46Al-8Nb (at%) with a fully lamellar microstructure was produced with horizontal centrifugal casting at ACCESS e.V. (Aachen, Germany). In this paper, for simplification, the alloys are named TiAlMn, TiAlCrMo, and TiAlNb, respectively. As can be seen in Figure 1a, TiAlMn (OT4-1) was characterized by equiaxed grains with lighter Mn-rich precipitates. TiAlCrMo (VT3-1) (Figure 1b) was a martensitic dual-phase $\alpha + \beta$ alloy, consisting of about 62vol% of α phase [44]. The lamellar microstructure of TiAlNb (Figure 1c) was composed of about 75vol% of γ -TiAl and about 25vol% of α_2 -Ti₃Al (lighter lamellas). Samples were cut from the ingots in the form of discs and quarter discs, 16–20 mm in diameter and 1.5–2.5 mm in thickness, then ground with emery papers up to 1200 grit and polished with Struers diamond suspensions (9, 3, and 1 μ grain sizes). Before coating deposition, the samples were washed in distilled water and degreased in acetone.

Table 1. Chemical compositions of the investigated alloys, declared by the manufacturer, and determined using EDS—energy-dispersive X-ray spectroscopy (in at least three spots).

Alloy	Ti [at%]	Al [at%]	Cr [at%]	Mn [at%]	Mo [at%]	Nb [at%]
Ti-5Al-2Mn (OT4-1)	93.0–96.6	3.0–4.5	-	1.7–2.3	-	-
EDS	92.0 \pm 1.8	4.4 \pm 1.3	-	3.2 \pm 1.0	-	-
Ti-12Al-2Cr-2Mo (VT3-1)	84.8–88.9	9.5–12.0	0.7–1.8	-	1.0–1.4	-
EDS	83.7 \pm 1.4	10.8 \pm 1.1	2.4 \pm 0.9	-	2.7 \pm 0.5	-
Ti-46Al-8Nb	46.1–46.4	45.9–46.3	-	-	-	7.6–7.9
EDS	51.7 \pm 3.9	39.7 \pm 3.4	-	-	-	8.6 \pm 0.4

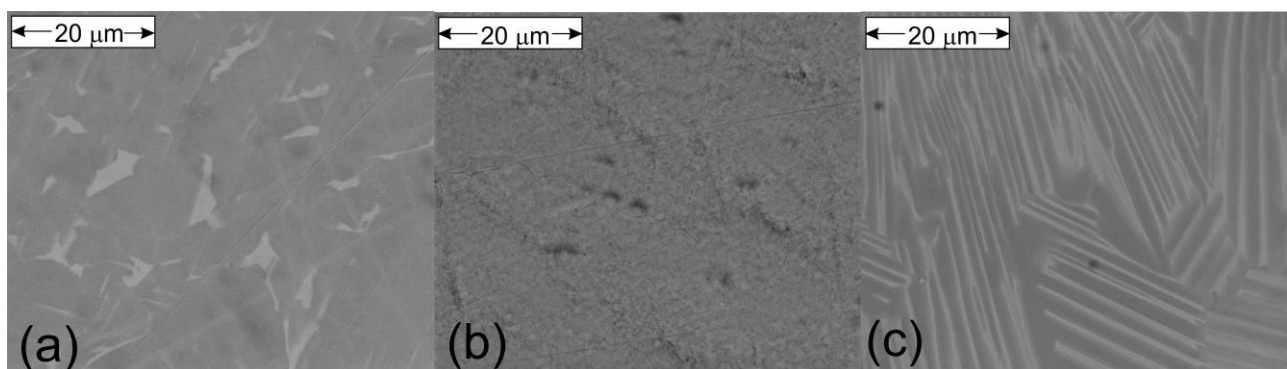


Figure 1. BE (backscattered electron) images of investigated alloys: (a) TiAlMn, (b) TiAlCrMo, (c) TiAlNb.

In the first step of the coating deposition, chromium was magnetron sputtered (WMK-50 magnetron gun supported by MF power supply) on alloy substrates. Cr deposition was conducted in a vacuum chamber (NP 501 A) for 1 h, under the following conditions: cathode current intensity 0.4–0.5 A, substrate temperature 50–100 °C, cathode effective power 0.3–0.5

kW. Argon flow was controlled by an MKS flow meter. In the second step, halide-activated pack cementation was used. The samples with Cr layers were immersed in a powder mixture composed of 25 wt% silicon (grain size not exceeding 40 μm) and 75 wt% alumina (grain size below 90 μm) and activated with cryolite (Na_3AlF_6) in an amount of 1.6 wt% relative to the mass of two main components (Si and Al_2O_3). The siliconizing process was conducted under a protective atmosphere of argon for 10 h at 850 $^\circ\text{C}$. The parameters of siliconization were selected based on our previous experience [45]. For comparison, samples without the Cr layer were siliconized in the same conditions. The coating deposition and testing routine is schematically presented in Figure 2.

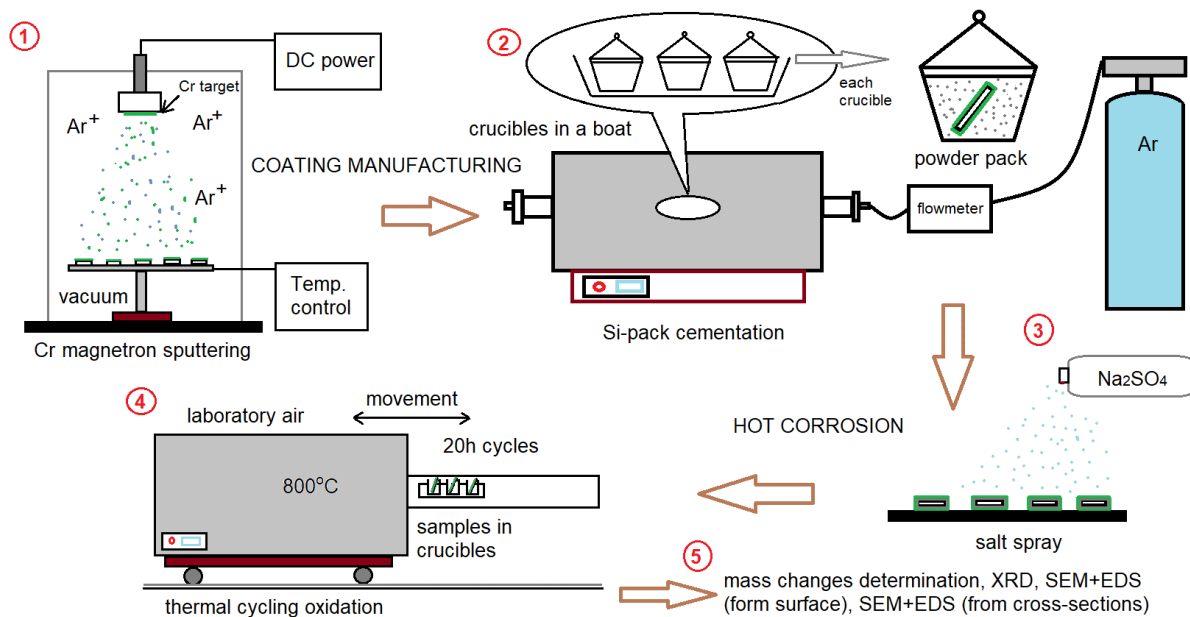


Figure 2. Scheme of Cr-Si coating deposition and processing. The numbers indicate the following stages.

Titanium alloys with and without coatings were tested under thermal cycling conditions at a temperature of 800 $^\circ\text{C}$ for up to 300 h. Each cycle consisted of the following steps: heating to 800 $^\circ\text{C}$ (rate of about 50 $^\circ\text{C}/\text{min}$), maintaining at 800 $^\circ\text{C}$ for 20 h, and cooling in laboratory air to 100 $^\circ\text{C}$ (rate of about 50 $^\circ\text{C}/\text{min}$). After next 20 min, the samples were stored in a desiccator for about 4 h. Before the tests, samples with and without coatings were immersed in a 10 wt% Na_2SO_4 aqueous solution, dried in air, stored in a desiccator for 2 h, and then weighed. The amount of salt deposited on the specimen surface did not exceed 1 mg/cm^2 . During the hot corrosion tests, the samples were kept in alumina crucibles, which allowed collection of the spalled material. The mass of each sample was determined using an electronic balance with a resolution of 0.1 mg. The post-test analysis included scanning electron microscopy (Nova Nano SEM 200, FEI Europe Company, Eindhoven, The Netherlands, equipped with energy-dispersive X-ray spectroscopy (EDS) and Merlin Gemini II, ZEISS, Oberkochen, Germany, equipped with a Quantax 800 microanalysis system—EDS, Bruker, Billerica, MA, USA) and X-ray diffraction analysis (Seifert FPM, Ahrensburg, Germany, XRD7, Cu X-ray tube, step size: 0.017). Scanning electron microscopy was used with a backscattered electron (BE) detector.

3. Results and Discussion

3.1. Coating Deposition

The simultaneous codeposition of Cr and Si using pack cementation is a difficult task because of thermodynamic limits (the partial pressures of chromium and silicon halides are different under the same conditions). Based on thermodynamic calculations, Rapp [46] proposed one possible solution to depositing Cr and Si, i.e., by using a mixture

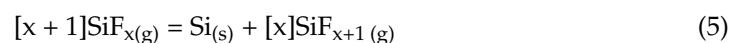
of two activators, NaF and NaCl. However, in our previous experiments, although the recommended mixture of activators was used, and the temperature and pack composition were optimized, the coatings on the titanium alloys were not satisfactory. Therefore, the intended Cr-Si coating was deposited by pack cementation realized in two steps: siliconizing (850 °C, 10 h, 1.6 wt% of Na₃AlF₆ as an activator) and chromizing (1050 °C, 10 h, 3 wt% CrCl₃ as an activator). When siliconizing was first conducted and followed by chromizing, the Ti-Si phases were predominant in the coating composition. Chromium was present only on the surface in the form of sintered powder. The only detected chromium phase was Cr₂Ti. It is likely that chromium was not soluble in the Ti-Si phases. According to the Ti-Si binary phase diagram [47] TiSi₂, TiSi, Ti₅Si₄, and Ti₃Si are fully stoichiometric silicide phases without solubility ranges. It also seems that Ti-Si phases have a higher thermodynamic stability than Cr-Si. Finally, the pack cementation process was changed and first chromizing and then siliconizing were conducted. Ti-Si and Cr-Si phases were found at the surface, but unfortunately, the obtained coatings were not uniform and, in some places, only islands enriched in chromium were recognized. Moreover, the temperature of 1050 °C appeared to be too high for the investigated titanium alloys, which underwent changes in their microstructures. The only solution was to deposit chromium using a different method at a lower temperature, and this was possible using magnetron sputtering. The results of the coating preparation are presented in Table 2 and Figure 3.

Table 2. Sample mass gains after each step of coating deposition.

Alloy	PVD Chromizing [mg/cm ²] Cr-Coating	CVD Siliconizing [mg/cm ²] Si-Coating	CVD Siliconizing after PVD [mg/cm ²] Cr-Si-Coating
TiAlMn	0.85 ± 0.09	1.75 ± 0.63	1.96 ± 0.26
TiAlCrMo	0.86 ± 0.14	1.97 ± 0.23	2.37 ± 0.27
TiAlNb	0.84 ± 0.16	1.60 ± 0.60	2.09 ± 0.90

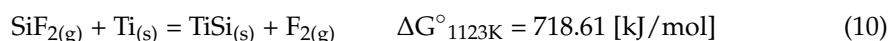
The averaged mass gains of the samples in relation to their surface area after each step of coating deposition are collected in Table 2. The values were calculated based on at least three samples for each step.

As can be seen in Table 2, for all the alloys, the first step of coating deposition caused a similar effect and the mass gains after chromium sputtering were around 0.9 mg/cm². The analysis of the cross-sections (Figure 3a) allowed us to conclude that the Cr layer had a uniform thickness of about 1.2–1.5 µm and adhered well to the substrate. Samples after only siliconization are shown in Figure 3b. The mass gains of the samples after siliconizing differed slightly—the highest (close to 2 mg/cm²) were those of TiAlCrMo (Table 2). The silicide layers had thicknesses between 10 and 18 µm. However, it is worth noting that the thicknesses of these coatings differed depending on the place of analysis. The siliconizing process was analyzed in detail in our previous paper [45]. In principle, siliconizing in a halide-activated pack mixture can be described by the following reactions [48]:



According to thermodynamic calculations [48], SiF₄ has the highest partial pressure in a pack activated by fluorides, but it could not react according to Reaction (5), because it was a silicon fluoride in its highest oxidation state and, therefore, could only participate in the transport of fluorine back to the powder pack. To check the most probable reactions,

selected standard Gibbs free energies at 850 °C were calculated based on the available thermodynamic data [49]:



It seems that the Ti-Si phases could be formed in the reactions with SiF_2 , and apparently the first phase to appear was TiSi; then, with an excess of silicon, it could transform into TiSi_2 . According to [45,46], after halide-activated siliconizing, the outermost coating layer was TiSi_2 , which is also in accordance with the results presented in the present paper. The EDS analysis at point 1 marked in Figure 3c confirms that the atomic ratio of Ti to Si was approximately 1:2. The TiSi_2 phase was also detected using XRD analysis (not presented here). Under the TiSi_2 layer, other Ti-Si phases are possible, namely TiSi and Ti_5Si_4 . As can be seen in Figure 3b, the silicide coatings on the TiAlMn and TiAlCrMo substrates are similar. The thickest TiSi_2 layer is followed by TiSi or Ti_5Si_4 . Close to the coating/alloy interface, small pores (Kirkendall porosity) are visible, which indicates that the main mechanism of coating growth was an outward diffusion of Ti. The silicide coating formed on TiAlNb (Figure 3c) has a slightly different morphology. Three main layers can be recognized: an outermost layer built of TiSi_2 , a middle layer—TiSi—with visible porosity, and an innermost layer, close to the coating/alloy interface, enriched in Al. The aluminum enrichment again confirms the contribution of an outward diffusion of titanium to the silicide coating growth. As explained in our previous paper [45], porosity in the intermediate layer is caused by the evaporation of aluminum segregating from the silicide phases. Niobium is also present in the silicide coating on TiAlNb, which is not surprising because niobium and silicon can form intermetallic phases [50]; however, since niobium is a slow diffuser in titanium aluminide phases [51], the amount of niobium silicides is smaller compared with that of titanium silicides.

The morphology and composition of the Cr-Si coatings presented in Figure 3c,d indicate that the coating growth mechanism was different and more complex than it was during the siliconizing of bare alloys. The outermost coating layer on all the alloys was built of chromium and silicon in a molar proportion close to 1:2, suggesting it was composed of crystals of the CrSi_2 phase. The CrSi_2 crystalline phase was indeed confirmed using XRD (Figure 3d). The CrSi_2 phase probably grew due to an inward diffusion of Si. Chromium remained in the outermost layer of the coating, so it could be treated as a marker, and its position allows one to guess that the predominant transport mechanisms were an inward diffusion of silicon accompanied by an outward diffusion of titanium. There are

not many papers in the literature about Cr and Si codeposited on titanium alloys using pack cementation. It was found that during the simultaneous deposition of Cr and Si on a Nb-Si composite, the coating was formed via sequential inward diffusion of Cr and Si and the pack mixture was activated with NH_4Cl [52]. In our experiment, the Cr-Si coatings deposited on the TiAlMn and TiAlCrMo alloys were uniform and composed of similar layers. However, in the case of the Cr-Si coating on TiAlNb, the thickness proportions between the Cr-Si top layer and the Ti-Si inner layer differed between the samples and the analyzed site. It is worth mentioning that when a thicker Ti-Si layer was detected, it was less porous in comparison with those after only siliconization, because aluminum evaporation was hindered by the Cr-Si layer. It is also possible that chromium reacted with the excess of aluminum (which did not react with silicon) and some Cr-Al intermetallic phases less volatile than aluminum appeared.

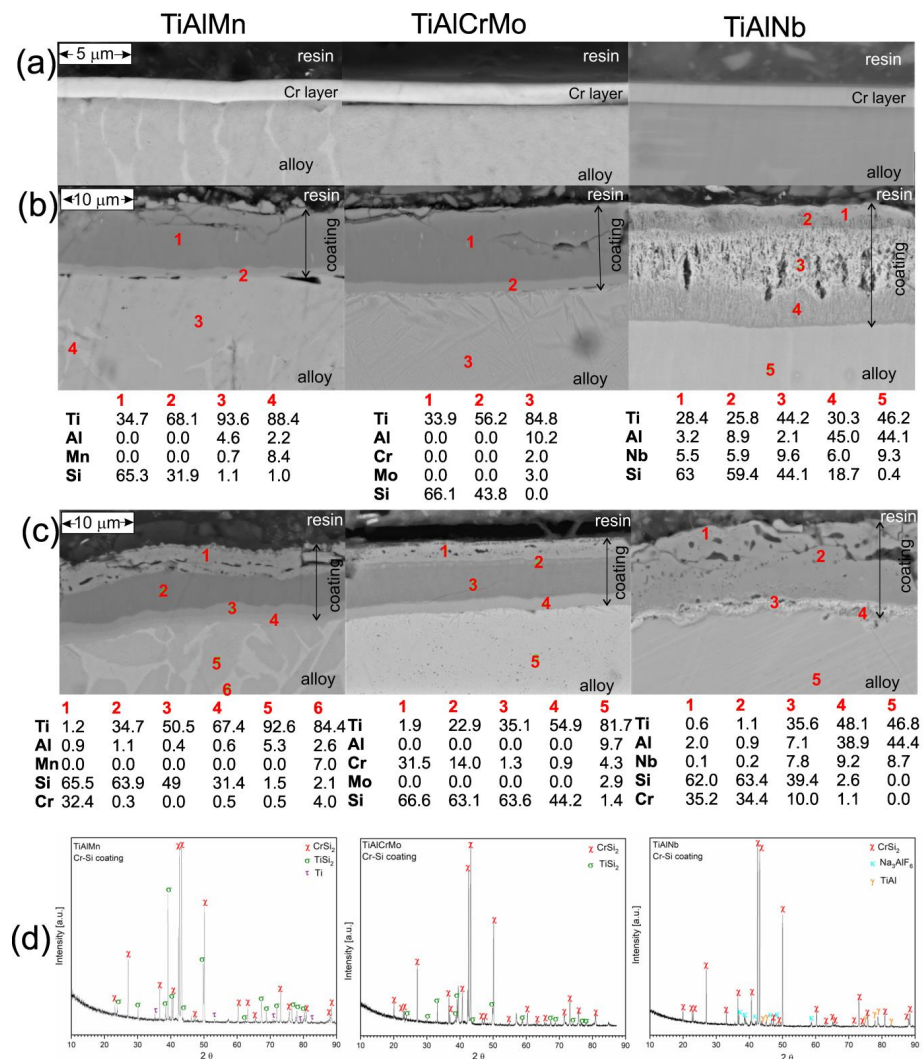


Figure 3. BE images of sample cross-sections after each step of coating manufacture: (a) after Cr magnetron sputtering; (b) after siliconizing of bare alloys with EDS analysis in the marked points, numbers 1–4; (c) after siliconizing of Cr-coated alloys with EDS analysis in the marked points (numbers 1–6); and (d) XRD pattern of samples after Cr and Si deposition. Alloy composition is given at the top.

3.2. Hot Corrosion Behavior of Uncoated Samples

The hot corrosion behavior of TiAlMn and TiAlNb alloys was investigated in our previous work [53]; therefore, in the present paper, only unpublished results are presented.

In Figure 4, mass changes in the samples during hot corrosion tests are collected. The gross mass changes (sample with the crucible) are shown only for those samples that underwent scale spallation. As can be seen in Figure 4, the most intensive degradation was registered for TiAlCrMo, and therefore the experiment was stopped after 100 h (5 cycles) to prevent complete destruction of the sample.

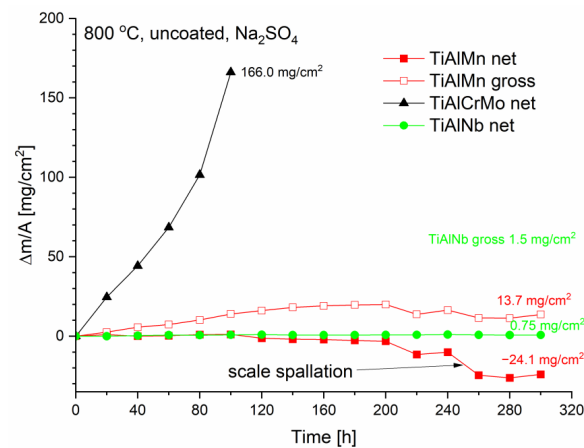


Figure 4. Net and gross mass changes of samples without coating after 300 h of oxidation at 800 °C with a Na₂SO₄ deposit (20 h cycles).

As can be seen in Figure 5b, the scale is thicker than 300 μm and built mostly of TiO₂ (Figure 5a). The intensive oxidation of TiAlCrMo and the porous structure of the scale were related to the presence of Mo in the alloy. According to the Mo-O phase diagram [54], the principal stable oxides are MoO₂ and MoO₃. Other nonstoichiometric Mo oxides with well-defined structures were also synthesized, but above 820 °C the only stable ones are MoO₂ and MoO₃ [55]. MoO₂ is violet, whereas MoO₃ is white, but it becomes yellow after heating. According to the vapor pressure calculations, below 600 °C, MoO₃ should be solid [55], but above 700 °C the partial pressure grows rapidly and reaches about 800 Pa at 800 °C [56], which is much more than 10 Pa, considered as the pressure above which the volatilization is significant [57]. Traces of the MoO₃ yellow deposit were also found at the crucible wall, as shown in Figure 5d.

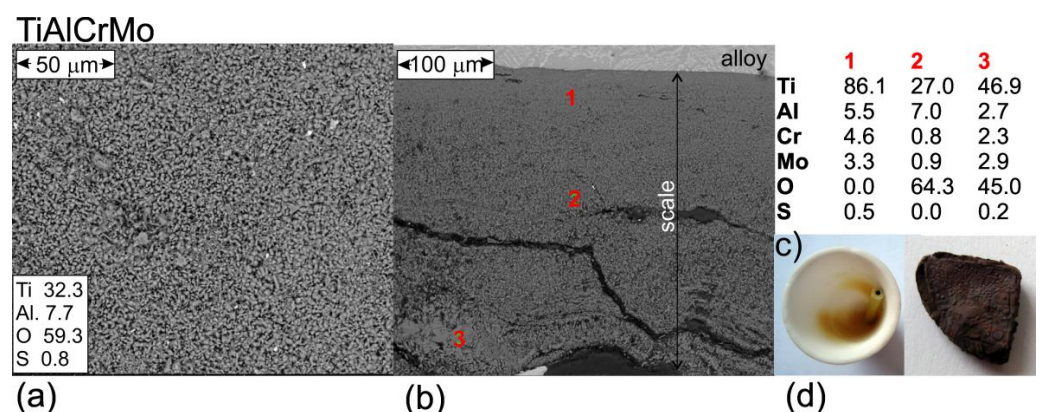


Figure 5. TiAlCrMo after 300 h of oxidation (20 h cycles) at 800 °C with a Na₂SO₄ deposit: (a) BE image of sample surface with EDS average analysis; (b) BE image of scale cross-section; (c) EDS analysis on the points marked (numbers 1–3) in (b); (d) digital picture of TiAlCrMo sample and crucible in which sample was oxidized.

The temperature of 800 °C is below the melting point of Na₂SO₄, but the influence of the salt deposit on the oxidation behavior is especially visible for TiAlNb. The final

mass gain at 800 °C was 0.75 mg/cm, which is about twice that of a sample without the salt deposit [58], but it is lower than we presented in our previous paper [53], because previously, Na₂SO₄ was redeposited after every 100 h of oxidation. Moreover, with the Na₂SO₄ deposit, the scale on TiAlNb was prone to spallation, which was not observed in the case of oxidation without the salt deposit. As was mentioned earlier, the main components of the scale formed on the TiAlNb alloy after hot corrosion in the presence of Na₂SO₄ were TiO₂ and Al₂O₃, accompanied by some crystalline niobates, AlNbO₄ and NaNbO₃, resulting from an acidic dissolution of alumina. The phase compositions of the TiAlMn and TiAlCrMo samples after oxidation with the Na₂SO₄ deposit are presented in Figures 6 and 7. For both figures, (a) is the composition of the sample surface whereas (b) is the composition of the spalled scale, powdered in a mortar before the analysis. As can be seen, the compositions of the scales are similar, their main component being TiO₂ (rutile). In the case of TiAlCrMo, TiO₂ was accompanied by Al₂O₃, because the alloy had a higher aluminum content. The XRD pattern in Figure 7a also confirmed the presence of MoO₃ in the spalled scale. Therefore it could be concluded that the catastrophic oxidation of the TiAlCrMo alloy was directly related to the evaporation of MoO₃. The phase compositions of the surface were more complex and differed between the alloys. The interpretation of diffractograms was difficult because of the large number of overlapping reflections. However, it seems that for both alloys, in some areas under the oxide scale, there were favorable conditions for the formation of nitrides. Indeed, reflections from TiN and AlN were detected. It is interesting that metastable CrO₂ was found in the scale formed on TiAlCrMo. CrO₂ is stable at a high oxygen pressure, and it easily decomposes into Cr₂O₃ under an ambient pressure [59]. On the other hand, chromium dioxide with a rutile-type tetragonal crystal structure [60] was successfully synthesized using a CVD process under ambient oxygen pressure on the TiO₂ and Al₂O₃ substrates [61,62]. Therefore, it is possible that in contact with the rutile phase, the most favorable chromium oxide was CrO₂ rather than Cr₂O₃. The CrO₂ and Cr₂O₃ oxides were also detected in the scale formed on a Ni-Cr-Mo alloy after a high-temperature corrosion test [63]. Interestingly, some reflections from titanates, aluminates, and even chromates were detected in the scales on the TiAlMn and TiAlCrMo alloys, as shown in Figures 6a and 7a. This indicates that even at temperatures lower than the melting point of Na₂SO₄, the decomposition reaction is possible:



The Na₂O can further react with oxides:



NaCrO₂ can be obtained in the reaction between Na₂CO₃ and Cr₂O₃ [64], but the analogous reaction is also probable:



Acidic dissolution of the main scale oxides (TiO₂ and Al₂O₃) was detrimental for the titanium alloys, because it accelerated oxidation and was the main reason for alloy degradation.

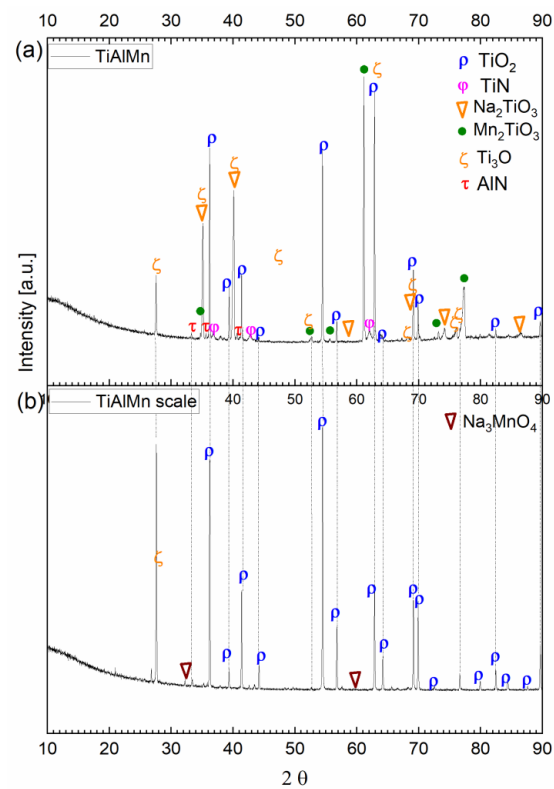


Figure 6. XRD analysis of uncoated TiAlMn alloy after 100 h of oxidation (20 h cycles) at 800 °C with a Na_2SO_4 deposit: (a) sample surface, (b) spalled scale.

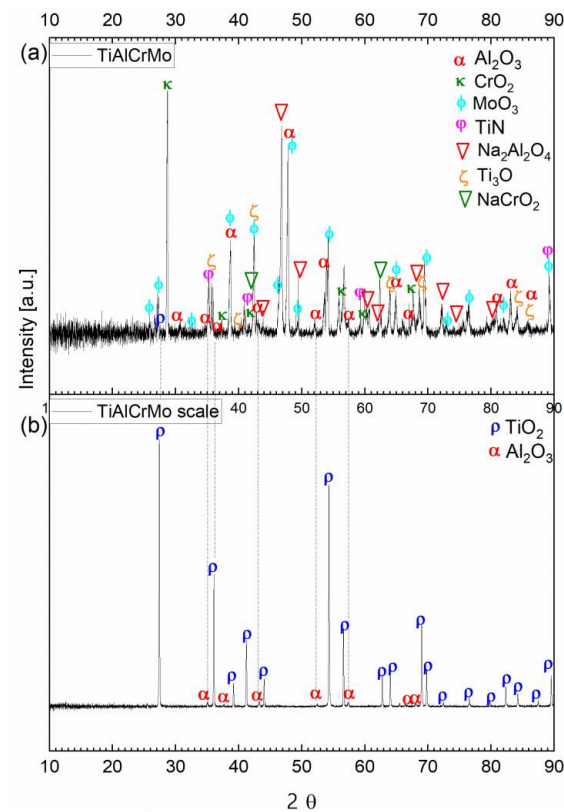


Figure 7. XRD analysis of uncoated TiAlCrMo alloy after 100 h of oxidation (20 h cycles) at 800 °C with a Na_2SO_4 deposit: (a) sample surface, (b) spalled scale.

3.3. Hot Corrosion Behavior of Si-Coated Samples

As can be seen in Figure 8, the net mass changes in the Si-coated samples were reduced compared with those presented in Figure 4. The positive influence of Si coating was mainly visible in the case of the samples with a lower Al content, TiAlMn and TiAlCrMo, for which the net mass gains were about 9 and 8 times lower, respectively. As was explained in our previous paper [45], this effect is related to the amorphous or partially crystalline layer of SiO₂ with embedded TiO₂ rutile crystals.

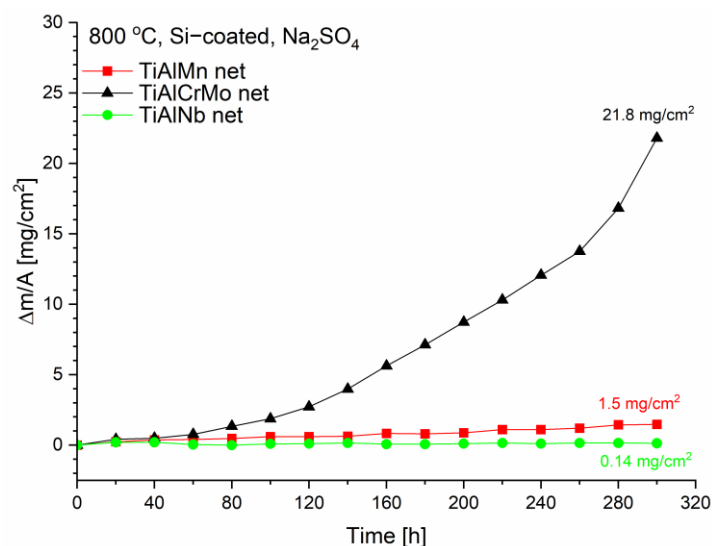


Figure 8. Net mass changes of Si-coated samples with a Na₂SO₄ deposit during 300 h of oxidation at 800 °C (20 h cycles).

The positive influence of SiO₂-containing coatings on the hot corrosion behavior of titanium alloys was already mentioned in the introduction section of this paper. The previous results are also confirmed here by the analyses in Figures 9 and 10. As can be seen in Figure 9, the compositions of the scales formed on the Si-coated TiAlMn and TiAlCrMo alloys were slightly different, but in general they consisted of similar phases. In the case of TiAlCrMo, the TiO₂ crystals were more visible on the surface (Figure 9a), and the oxygen penetration was deeper, spreading over the entire coating thickness (Figure 9c). Small nitride precipitates were also observed close to the scale/alloy interface. In the case of TiAlMn, the nitrogen profile followed the titanium profile, which suggested the occurrence of titanium nitride, and this was eventually confirmed with the XRD analysis (Figure 10a). The EDS profiles for the TiAlMn samples also indicated sulfur in the middle of the scale layer. Sulfide phases were not identified on the XRD pattern in Figure 10a, but their presence is not excluded, because the corresponding reflections could have been overlapped by those from other phases and some sulfides could have been present in the scale only locally, in the middle part, where the oxygen pressure was low enough. It could be concluded from Figure 9b that the morphology of the Si coating changed after the hot corrosion test and was no longer layered, but consisted of a mixture of TiO₂ (rutile), SiO₂ (mainly quartz and a small amount of cristobalite), and the remaining titanium silicide. The EDS profile of the Si-coated TiAlNb alloy indicated the presence of Al in the middle part of the coating, which was related to the formation of Al₂O₃, confirmed using the XRD analysis in Figure 10c. As indicated in Figure 10c, a minor sodium niobate phase was also detected, similar to the case of the uncoated alloy.

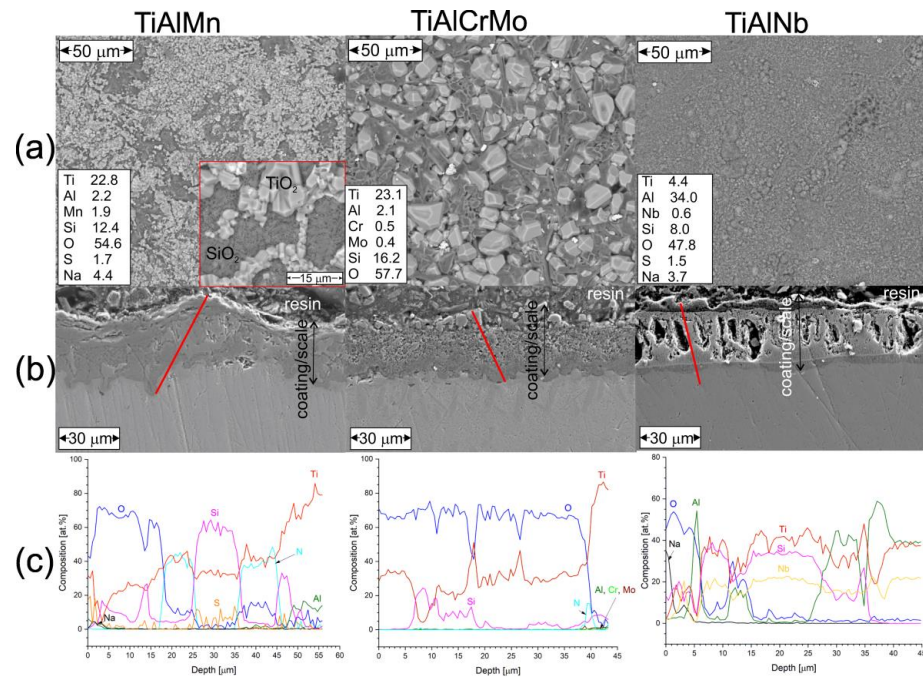


Figure 9. Si-coated alloys after 300 h of oxidation (20 h cycles) at 800 °C with a Na₂SO₄ deposit: (a) BE images of sample surface with EDS average analysis (for TiAlMn alloy, a higher magnification of the surface is shown in the red frame); (b) SE (secondary electron) images of cross-sections with the EDS line analysis marked in red; (c) EDS composition of scale/coating along lines marked in (b). Alloy composition is given at the top.

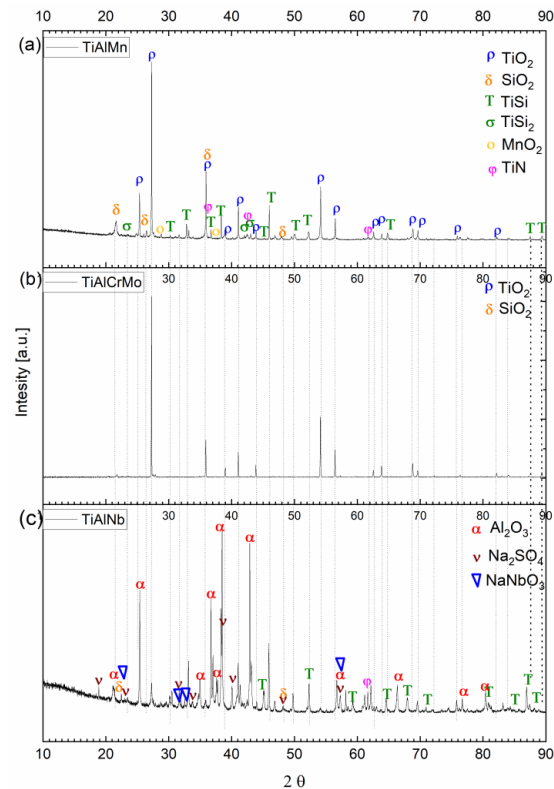


Figure 10. XRD analysis of Si-coated alloys after 300 h of oxidation (20 h cycles) at 800 °C with a Na₂SO₄ deposit. Alloy composition is given in the top-left corner.

3.4. Hot Corrosion Behavior of (Cr, Si)-Coated Samples

The main idea behind the Cr-Si coating was to improve the well-known positive influence of silicon on the oxidation and hot corrosion behavior of titanium alloys and achieve a synergistic effect. As can be seen in Figure 11, the net mass changes in the samples were again reduced in comparison with the Si-coated ones (Figure 8), and mass losses were even registered. The mass losses were attributed to spallation of the salt deposit. A small amount of white salt crystals was found in the crucibles. It could be concluded that the salt was less reactive in contact with the Cr-Si coating.

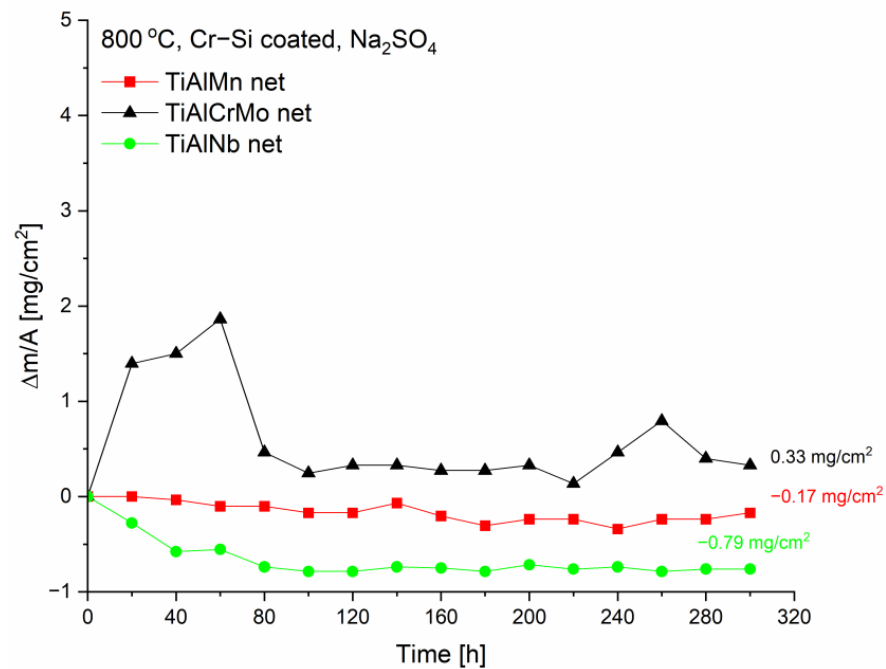
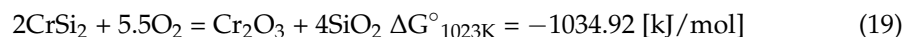


Figure 11. Net mass changes of (Cr, Si)-coated samples after 300 h of oxidation at 800 °C with a Na₂SO₄ deposit (20 h cycles).

In the case of TiAlCrMo, the small mass gain was probably due to the local growth of TiO₂ crystals visible in Figure 12a. Based on the average composition of the surface in Figure 12a, it could be concluded that SiO₂ was the predominant component of the scale. It should be mentioned that SiO₂ was accompanied only by traces of TiO₂, which is the main advantage of the Cr-Si coating. This significant reduction in TiO₂ growth is related to the Cr-Si top coating layer, which was oxidized preferentially according to the following reaction:



Gibbs free energy was calculated at 800 °C based on the thermodynamic data in [49].

The analyses of the cross-sections in Figure 12b indicate that for all the alloys, the top layer of the scale was composed of SiO₂. In the case of TiAlMn, the layer was thick and partially crystalline, as confirmed by clear reflections from SiO₂ (quartz and cristobalite). The SiO₂ layer on the coated TiAlCrMo was thinner, but it might have been damaged during the cross-section preparation. The Si-O layer on the coated TiAlNb appears relatively thick in Figure 12c, but the reflections from SiO₂ in Figure 13c are hardly visible, so it was probably an amorphous Si-O layer. For all the alloys, below the SiO₂ layer, a thin layer of CrSi₂ was still present. The amount of CrSi₂ was small because it was partially consumed during oxidation. However, it seems that the second product of CrSi₂ oxidation disappeared from the coating. Traces of Cr₂O₃ were detected only for the TiAlMn alloy. According to Reaction (19), the amount of Cr₂O₃ should be four times lower than that of SiO₂, but a

detectable quantity of chromium oxide was still expected. The evaporation of Cr₂O₃ is well described in the literature [65,66] but is mainly related to the presence of water vapor and the formation of CrO₂(OH)₂, according to the following reaction:

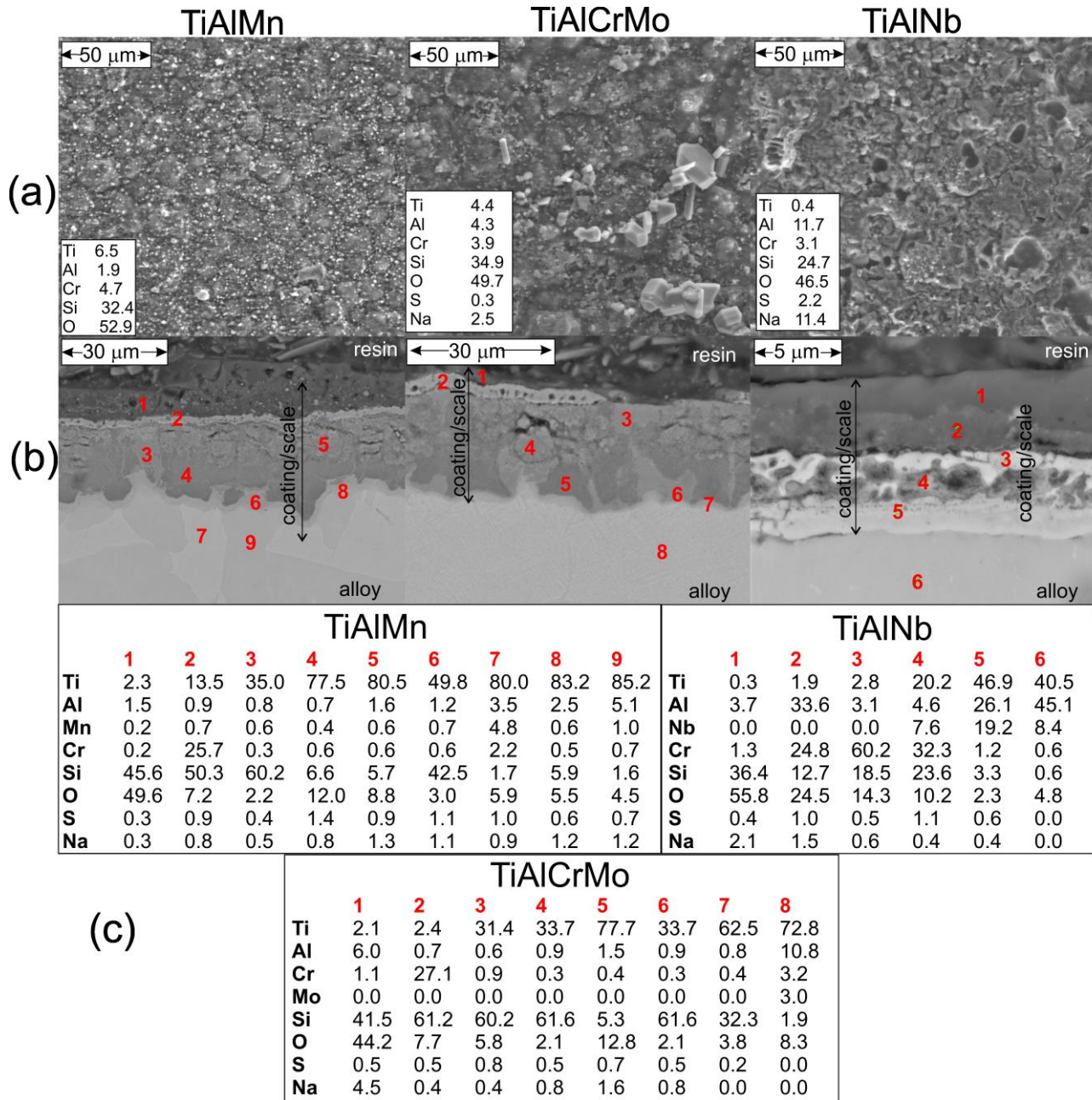
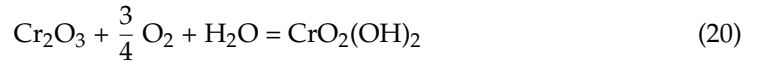


Figure 12. (Cr, Si)-coated alloys after 300 h of oxidation (20 h cycles) at 800 °C with a Na₂SO₄ deposit: (a) BE images of sample surface with EDS average analysis, (b) BE images of cross-sections with the EDS points marked as numbers, (c) EDS analysis on the points marked as numbers 1–9 in (b). Alloy composition is given at the top.

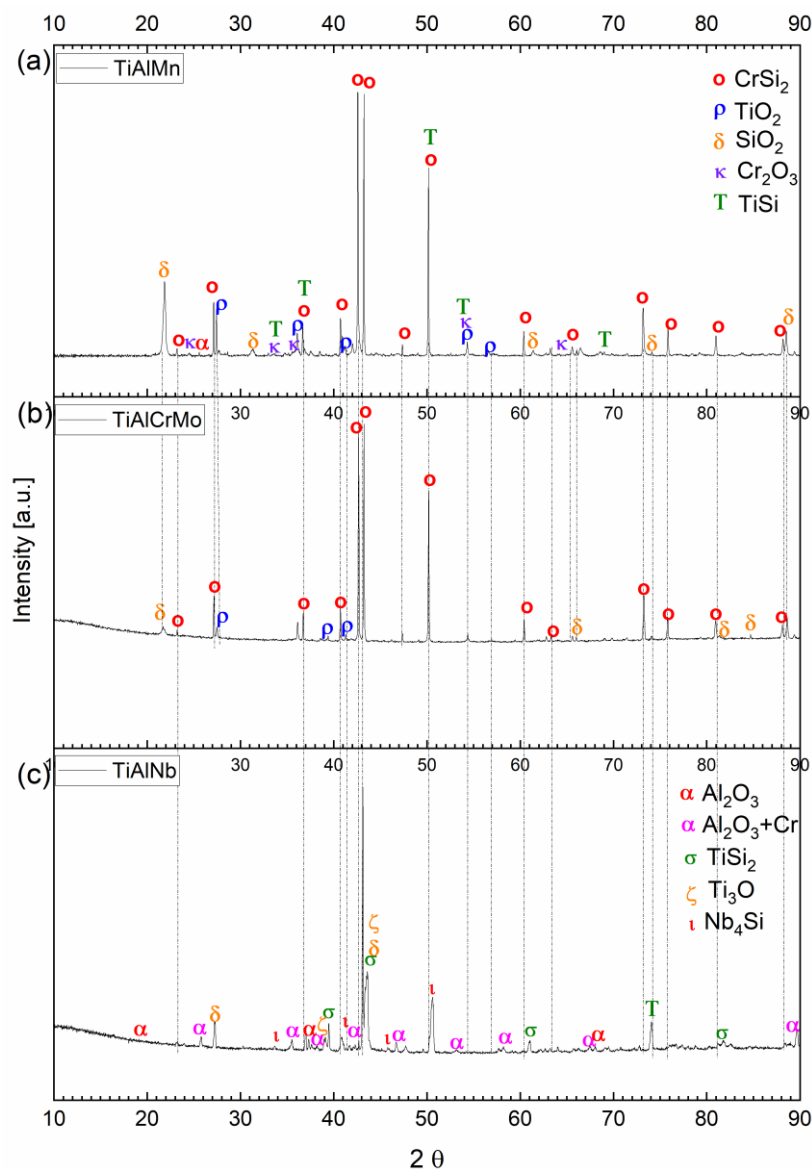


Figure 13. XRD analysis of (Cr, Si)-coated alloys after 300 h of oxidation (20 h cycles) at 800 °C with Na_2SO_4 deposit. Alloy composition is given in the top-left corner.

In the experiment described here, the samples were oxidized in laboratory air which was naturally saturated with water vapor. Moreover, the salt deposit was applied as a water solution, and even after drying, some amounts of water probably remained on the surface. The effect of $\text{CrO}_2(\text{OH})_2$ evaporation was for example observed in the case of Ni-Cr coatings oxidized in air containing H_2O [67]. The evaporation of chromium could also explain the mass losses visible in Figure 11. The loss of chromium is not a positive effect, but on the other hand, it can have some positive influence by shifting the CrSi_2 oxidation reaction to the right side and facilitating the formation of SiO_2 .

The structure of the Cr-Si coating after oxidation in the presence of Na_2SO_4 was similar for alloys with a lower aluminum content, but it was different for TiAlNb. In the latter case, under the thick and mainly amorphous SiO_2 layer, there was an Al-rich layer (Figure 12b), which consisted of Al_2O_3 according to the analysis in Figure 13c. It is interesting to note that the main part of Al_2O_3 was doped with chromium and the resulting phase had the following composition: $(\text{Al}_{0.948}\text{Cr}_{0.052})_2\text{O}_3$. It is known that Al_2O_3 and Cr_2O_3 are isostructural (hexagonal systems), and Al^{3+} and Cr^{3+} have similar ionic radii and at a high temperature can form a solid solution in the entire composition range [68]. The

properties of the $\text{Al}_2\text{O}_3\text{-Cr}_2\text{O}_3$ solid solution depend on the composition and are described in detail in another paper [69]. The $(\text{Al}_{0.948}\text{Cr}_{0.052})_2\text{O}_3$ -containing layer can be regarded as the secondary barrier against the hot-salt attack of the TiAlNb alloy. Moreover, the remaining titanium silicide layers for all investigated alloys could perform as an additional source of silicon for the formation of SiO_2 .

An interesting observation can be made about the Cr-Si coating for the TiAlNb alloy. Due to the titanium's outward diffusion and because niobium is the slower diffuser in the TiAlNb system, the layer enriched in niobium was formed (Figure 12c), as shown at point 5. As follows from the EDS analysis, the layer was mainly built of titanium, aluminum, and silicon in molar proportions close to 2:1:1, suggesting the Ti_2AlNb phase.

To summarize, the Cr-Si coating was the most efficient and promising for the protection of titanium alloys against oxidation in presence of a Na_2SO_4 deposit. Even though the role of chromium was not direct and only traces of Cr_2O_3 were found in the scale, the oxidation of CrSi_2 produced thicker SiO_2 layers, which could effectively protect the alloy for a longer time. Additionally, in the case of TiAlNb, chromium promoted the formation of the Al_2O_3 oxide. Finally, the inner coating layer, Ti-Si, for all the alloys could be treated as a reservoir of silicon for the SiO_2 layer recovery. The possible Cr-Si coating behavior during the hot corrosion test is presented schematically in Figure 14.

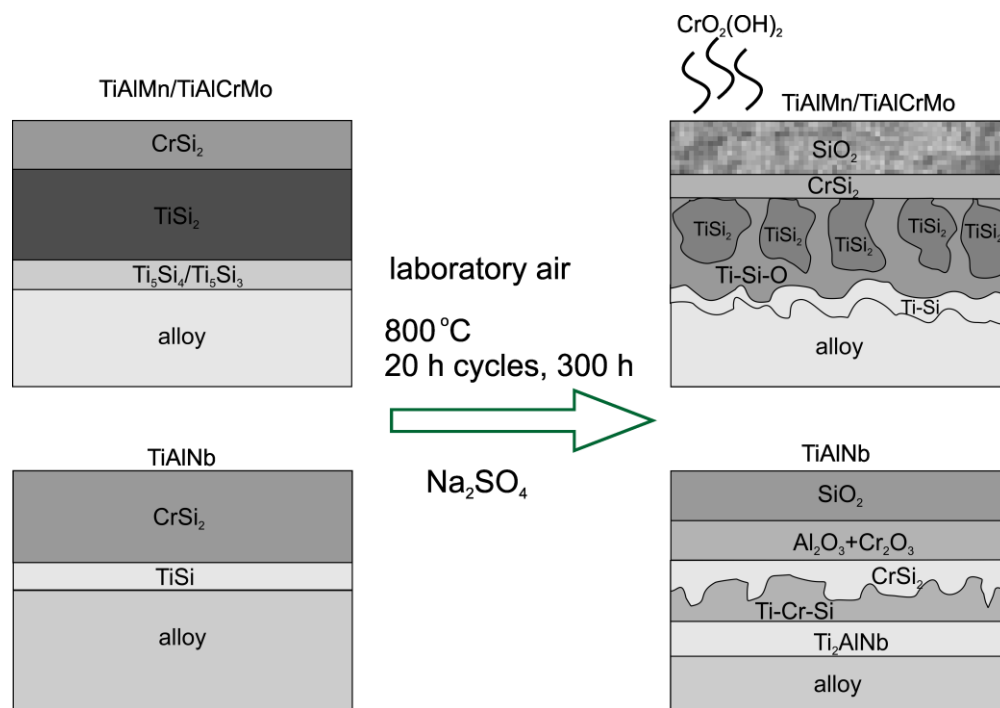


Figure 14. Scheme of Cr-Si-coated titanium alloys' oxidation in the presence of Na_2SO_4 deposit.

4. Conclusions

A multicomponent coating containing chromium and silicon was successfully obtained at the relatively low temperature of 850 °C in a two-step process comprising the deposition of Cr using magnetron sputtering and Si using pack cementation. The resulting coating was mainly built of silicide layers: CrSi_2 on the top, followed by TiSi_2 , and close to the alloy/coating interface, some lower Ti-silicides. The uncoated and coated alloys were oxidized in laboratory air in thermal cycling conditions (20 h) with a Na_2SO_4 salt deposit. The protectiveness of the Si and Cr-Si coatings evidenced the superiority of the latter. In the case of the Cr-Si coatings, the synergistic effect of Cr and Si in protecting titanium alloys from Na_2SO_4 -induced hot corrosion was proved and attributed to the following:

- Easier formation of a thicker and more uniform SiO₂ barrier layer resulting from the oxidation of CrSi₂;
- Cr-promoted growth of an Al₂O₃-rich inner layer of the scale in the case of the titanium aluminide alloy, TiAlNb;
- Better stability of the Cr-Si coatings in thermal cycling conditions and the progressive release of silicon, owing to the multilayer and multiphase composition.

Funding: This work was supported by a subsidy from the Ministry of Education and Science for the AGH University of Kraków (Project No 16.16.160.557).

Data Availability Statement: Data will be made available upon reasonable request.

Acknowledgments: The author acknowledges the contribution of Krzysztof Mars from the Faculty of Materials Science and Ceramics, AGH University of Krakow, who deposited the chromium layer with magnetron sputtering.

Conflicts of Interest: The author declares no conflict of interest.

References

1. Amigó-Borrás, V.; Lario-Femenía, J.; Amigó-Mata, A.; Vicente-Escuder, A. Titanium, Titanium Alloys and Composites. In *Encyclopedia of Materials: Metals and Alloys*; Caballero, F.G., Ed.; Elsevier: Amsterdam, The Netherlands, 2022; pp. 179–199. [[CrossRef](#)]
2. Mouritz, A.P. Titanium Alloys for Aerospace Structures and Engines. In *Introduction to Aerospace Materials*; Mouritz, A.P., Ed.; Woodhead Publishing: Cambridge, UK, 2012; Chapter 9; pp. 202–223. [[CrossRef](#)]
3. Polmear, I.; StJohn, D.; Nie, J.F.; Qian, M. (Eds.) Titanium Alloys. In *Light Alloys*; Butterworth-Heinemann: Oxford, UK, 2017; Chapter 7; pp. 369–460. [[CrossRef](#)]
4. Kermanpur, A.; Sepehri Amin, H.; Ziaei-Rad, S.; Nourbakhshnia, N.; Mosaddeghfar, M. Failure analysis of Ti6Al4V gas turbine compressor blades. *Eng. Fail. Anal.* **2008**, *15*, 1052–1064. [[CrossRef](#)]
5. Xu, K.; Wang, J.; Gao, Y.; Yang, F.; Pan, Y. Deformation measurement and simulation of Ti-6Al-4V blades induced by shot peening process. *Int. J. Adv. Manuf. Technol.* **2023**, *126*, 5017–5032. [[CrossRef](#)]
6. Yan, Z.; Zhu, L.; Yang, Z.; Xue, P. Study on the geometrical dimensions and mechanical properties of Ti-6Al-4V alloy blade by laser metal deposition. *Int. J. Adv. Manuf. Technol.* **2021**, *114*, 695–707. [[CrossRef](#)]
7. Agarwal, K.M.; Singhal, A.; Kapoor, A.; Bhatia, D. Simulated analysis of Ti-6Al-4V processed through equal channel angular pressing for biomedical applications. *Mater. Sci. Energy Tech.* **2021**, *4*, 290–295. [[CrossRef](#)]
8. Rodriguez, G.M.; Bowen, J.; Zelzer, M.; Stamboulis, A. Selective modification of Ti6Al4V surfaces for biomedical applications. *RSC Adv.* **2020**, *10*, 17642–17652. [[CrossRef](#)]
9. Milovanović, A.; Sedmak, A.; Grbović, A.; Mijatović, T.; Čolić, K. Design Aspects of Hip Implant Made of Ti-6Al-4V Extra Low Interstitials Alloy. *Procedia Struct. Integr.* **2020**, *26*, 299–305. [[CrossRef](#)]
10. Kustono, D.; Andoko, R.W.; Puspitasari, P.; Kurniawan, G.A.; Putra, A.D. Simulation of knee implants made of Ti6Al4V material during walking. *MATEC Web Conf.* **2018**, *204*, 07015. [[CrossRef](#)]
11. De la Garza-Ramos, M.A.; Estupiñan-Lopez, F.H.; Gaona-Tiburcio, C.; Beltrán-Novelo, L.G.; Zambrano-Robledo, P.; Cabral-Miramontes, J.; Almeraya-Calderón, F. Electrochemical Behavior of Ti6Al4V Alloy Used in Dental Implants Immersed in *Streptococcus gordonii* and *Fusobacterium nucleatum* Solutions. *Materials* **2020**, *13*, 4185. [[CrossRef](#)] [[PubMed](#)]
12. Gurrappa, I. Characterization of titanium alloy Ti-6Al-4V for chemical, marine and industrial applications. *Mater. Charact.* **2003**, *51*, 131–139. [[CrossRef](#)]
13. Zheng, X.; Zhuang, X.; Lei, Y.; Chu, Z.; Xu, J.; Gao, L.; Sun, X. Corrosion Behavior of the Ti-6Al-4V Alloy in Sulfate-Reducing Bacteria Solution. *Coatings* **2020**, *10*, 24. [[CrossRef](#)]
14. Chen, W.; Zhang, D.; Wang, E.; Yan, F.; Xiang, L.; Xie, Z. Corrosion Degradation Behaviors of Ti6Al4V Alloys in Simulated Marine Environments. *Coatings* **2022**, *12*, 1028. [[CrossRef](#)]
15. Williams, J.C.; Boyer, R.R. Opportunities and Issues in the Application of Titanium Alloys for Aerospace Components. *Metals* **2020**, *10*, 705. [[CrossRef](#)]
16. Takahashi, K.; Mori, K.; Takebe, H. Application of Titanium and its Alloys for Automobile Parts. *MATEC Web Conf.* **2020**, *321*, 02003. [[CrossRef](#)]
17. Singh, P.; Pungotra, H.; Kalsi, N.S. On the characteristics of titanium alloys for the aircraft applications. *Mater. Today Proc.* **2017**, *4*, 8971–8982. [[CrossRef](#)]
18. Bewlay, B.P.; Nag, S.; Suzuki, A.; Weimer, M.J. TiAl alloys in commercial aircraft engines. *Mater. High Temp.* **2016**, *33*, 549–559. [[CrossRef](#)]
19. Moore, S. 3D Printing Titanium in Aerospace Manufacturing Applications. AZOM 2022. 24 September. Available online: <https://www.azom.com/article.aspx?ArticleID=19272> (accessed on 24 April 2023).

20. Bewlay, B.; Weimer, M.; Kelly, T.; Suzuki, A.; Subramanian, P. The Science, Technology, and Implementation of TiAl Alloys in Commercial Aircraft Engines. *MRS Proc.* **2013**, *1516*, 49–58. [CrossRef]
21. Smialek, J.L.; Jacobson, N.S. Oxidation of High-Temperature Aerospace Materials. In *High Temperature Materials and Mechanisms*, 1st ed.; Bar-Cohen, Y., Ed.; CRC Press Taylor & Francis Group: Boca Raton, FL, USA, 2014; Chapter 5; pp. 95–162. [CrossRef]
22. Gurrappa, I.; Yashwanth, I.V.S.; Mounika, I.; Murakami, H.; Kuroda, S. The Importance of Hot Corrosion and Its Effective Prevention for Enhanced Efficiency of Gas Turbines. In *Gas Turbines—Materials, Modeling and Performance*; Gurrappa, I., Ed.; InTechOpen: London, UK, 2015; Chapter 3. [CrossRef]
23. Rapp, R.A.; Zhang, Y.S. Hot corrosion of materials: Fundamental studies. *JOM* **1994**, *46*, 47–55. [CrossRef]
24. Yang, P.; Bu, Z.; An, Y.; Zhou, H.; Li, Y.; Chen, J. A systematic study on Na₂SO₄-induced hot corrosion behavior of plasma-sprayed La₂(Zr_{0.75}Ce_{0.25})₂O₇ coating. *Surf. Coat. Tech.* **2022**, *429*, 127979. [CrossRef]
25. ASCENT Environmental Cost-Benefit Analysis of Ultra Low Sulfur Jet Fuels. Available online: <https://ascent.aero/partner-27> (accessed on 14 March 2023).
26. Hu, S.; Finklea, H.; Liu, H. A review on molten sulfate salts induced hot corrosion. *J. Mater. Sci. Technol.* **2021**, *90*, 243–254. [CrossRef]
27. Waeytens, M.; Syed, A.U.; Roberts, T.; Martinez, F.D.; Gray, S.; Nicholls, J.R. A microscopy study of nickel-based superalloys performance in type I hot corrosion conditions. *Mater. High Temp.* **2023**. [CrossRef]
28. Valenti, L.E.; Bonnet, L.V.; Galiano, M.R.; Giacomelli, C.E. A simple strategy to prepare hybrid coating on titanium (Ti6Al4V). *Surf. Coat. Tech.* **2022**, *431*, 128017. [CrossRef]
29. Sánchez-Bodón, J.; Andrade Del Olmo, J.; Alonso, J.M.; Moreno-Benítez, I.; Vilas-Vilela, J.L.; Pérez-Álvarez, L. Bioactive Coatings on Titanium: A Review on Hydroxylation, Self-Assembled Monolayers (SAMs) and Surface Modification Strategies. *Polymers* **2021**, *4*, 165. [CrossRef]
30. Yang, L.; Gao, F.; Zhou, Z.; Jia, Y.; Du, Y.; Wang, J.; Qiao, Y.; Zhu, S.; Wang, F. Oxidation behavior of the AlN coatings on the TiAl alloy at 900 °C. *Corros. Sci.* **2023**, *211*, 110891. [CrossRef]
31. Gruner, H. Thermal Spray Coatings on Titanium. In *Titanium in Medicine. Engineering Materials*; Springer: Berlin/Heidelberg, Germany, 2001. [CrossRef]
32. Catauro, M.; Barrino, F.; Bononi, M.; Colombini, E.; Giovanardi, R.; Veronesi, P.; Tranquillo, E. Coating of Titanium Substrates with ZrO₂ and ZrO₂-SiO₂ Composites by Sol-Gel Synthesis for Biomedical Applications: Structural Characterization, Mechanical and Corrosive Behavior. *Coatings* **2019**, *9*, 200. [CrossRef]
33. Jacobs, M.; De Vos, Y.; Middelkoop, V. Thickness controlled SiO₂/TiO₂ sol-gel coating by spraying. *Open Ceram.* **2021**, *6*, 100121. [CrossRef]
34. Costa, M.Y.P.; Venditti, M.L.R.; Cioffi, M.O.H.; Voorwald, H.J.C.; Guimarães, V.A.; Ruas, R. Fatigue behavior of PVD coated Ti-6Al-4V alloy. *Int. J. Fatigue* **2011**, *33*, 759–765. [CrossRef]
35. Ewald, A.; Glückermann, S.K.; Thull, R.; Gbureck, U. Antimicrobial titanium/silver PVD coatings on titanium. *BioMed. Eng. Online* **2006**, *5*, 22. [CrossRef] [PubMed]
36. Delmas, M.; Ucar, M.; Ressler, L.; Pons, M.; Vahlas, C. MOCVD processed platinum–aluminum coatings on titanium alloys. *Surf. Coat. Tech.* **2004**, *188–189*, 49–54. [CrossRef]
37. Wu, L.K.; Wu, J.J.; Wu, J.Y.; Yan, H.Y.; Jiang, M.Y.; Cao, F.H. Hot corrosion behavior of electrodeposited SiO₂ coating on TiAl alloy. *Corros. Sci.* **2020**, *174*, 108827. [CrossRef]
38. Pambudi, M.J.; Basuki, E.A.; Prajitno, D.H. Improving Hot Corrosion Resistance of Two Phases Intermetallic Alloy α₂-Ti₃Al/γ-TiAl with Enamel Coating. *AIP Conf. Proc.* **2017**, *1805*, 070003. [CrossRef]
39. Hu, Y.T.; Zheng, L.; Yan, H.J.; Wu, L.K.; Lin, X.J.; Cao, F.H.; Jiang, M.Y. Improving hot corrosion resistance of aluminized TiAl alloy by anodization and pre-oxidation. *Trans. Nonferrous Met. Soc. China* **2021**, *3*, 193–206. [CrossRef]
40. Li, Y.Q.; Xie, F.Q.; Yang, S.L. Microstructure and hot corrosion resistance of Si-Al-Y coated TiAl alloy. *J. Cent. South Univ.* **2020**, *27*, 2530–2537. [CrossRef]
41. Rubacha, K.; Godlewska, E.; Mars, K. Behaviour of a silicon-rich coating on Ti-46Al-8Ta (at. %) in hot-corrosion environments. *Corros. Sci.* **2017**, *118*, 158–167. [CrossRef]
42. Zhang, M.; Feng, Y.; Wang, Y.; Niu, Y.; Xin, L.; Li, Y.; Su, J.; Zhu, S.; Wang, F. Corrosion Behaviors of Nitride Coatings on Titanium Alloy in NaCl-Induced Hot Corrosion. *Acta Metall. Sin.* **2021**, *34*, 1434–1446. [CrossRef]
43. Mitoraj, M.; Mars, K.; Matuła, M.; Godlewska, E. Hot corrosion behaviour of Cr-Si coated titanium alloys. *Ann. Chim. Mat.* **2015**, *39*, 141–148. [CrossRef]
44. Ziaja, W.; Motyka, M.; Kubiak, K.; Sieniawski, J. Primary creep behaviour of two-phase titanium alloy with various microstructure. *Arch. Metall. Mater.* **2016**, *61*, 683–688. [CrossRef]
45. Mitoraj-Królikowska, M.; Godlewska, E. Silicide coatings on Ti-6Al-1Mn (at.%) alloy and their oxidation resistance. *Surf. Coat. Tech.* **2018**, *334*, 491–499. [CrossRef]
46. Harper, M.A.; Rapp, R.A. Codeposited Chromium and Silicon Diffusion Coatings for Fe-Base Alloys via Pack Cementation. *Oxid. Met.* **1994**, *42*, 303–333. [CrossRef]
47. Massalski, T.B.; Okamoto, H.; Subramanian, P.R.; Kacprzak, L. (Eds.) *Binary Alloy Phase Diagrams*, 2nd ed.; ASM International: Almere, The Netherlands, 1990. [CrossRef]

48. Cockeram, B.V.; Rapp, R.A. The Kinetics of Multilayered Titanium-Silicide Coatings Grown by the Pack Cementation Method. *Metal. Mater. Trans. A* **1995**, *26A*, 777–791. [[CrossRef](#)]
49. Barin, I.; Knacke, O.; Kubaschewski, O. *Thermochemical Properties of Inorganic Substances: Supplement*; Springer: Berlin, Germany, 1977; Volume 1.
50. Prasad, S.; Paul, A. Growth mechanism of phases by interdiffusion and diffusion of species in the niobium–silicon system. *Acta Mater.* **2011**, *59*, 1577–1585. [[CrossRef](#)]
51. Hu, D.; Huang, A.J.; Wu, X. On the massive phase transformation regime in TiAl alloys: The alloying effect on massive/lamellar competition. *Intermetallics* **2007**, *15*, 327–332. [[CrossRef](#)]
52. Yuan, B.; Li, Y.; Qiao, M.; Zhou, C. Vapor phase codeposition of Cr and dSi on Nb-base insitu composites by pack cementation process. *Prog. Nat. Sci. Mater. Inter.* **2013**, *23*, 198–204. [[CrossRef](#)]
53. Mitoraj-Królikowska, M.; Godlewska, E. Hot corrosion behaviour of ($\gamma + \alpha_2$)-Ti-46Al-8Nb (at. %) and α -Ti-6Al-1Mn (at. %) alloys. *Corros. Sci.* **2017**, *115*, 18–29. [[CrossRef](#)]
54. Brewer, L.; Lamoreaux, R.H. The Mo-O System (Molybdenum-Oxygen). *Bull. Alloy. Phase Diagr.* **1980**, *1*, 85–89. [[CrossRef](#)]
55. Micco, G.; Nassini, H.E.; Bohé, A.E. Kinetics of Molybdenum Oxidation Between 375 and 500 °C. In *Molybdenum and its Compounds*; Saji, V.S., Lopatin, S.I., Eds.; Nova Science Publishers: Hauppauge, NY, USA, 2014; Chapter 17; pp. 313–338.
56. Yang, Y.; Pu, H.; Di, J.; Zhang, S.; Hu, J.; Zang, Y.; Gao, C.; Chen, C. Influences of temperature gradient and distance on the morphologies of MoS₂ domains. *AIP Adv.* **2018**, *8*, 085218. [[CrossRef](#)]
57. Chang, Y.N.; Wei, F.I. High-temperature chlorine corrosion of metals and alloys. *J. Mater. Sci.* **1991**, *26*, 3693–3698. [[CrossRef](#)]
58. Mitoraj, M.; Godlewska, E.M. Oxidation of Ti-46Al-8Ta in air at 700 °C and 800 °C under thermal cycling conditions. *Intermetallics* **2013**, *34*, 112–121. [[CrossRef](#)]
59. Si, P.Z.; Wang, H.X.; Jiang, W.; Lee, J.G.; Choi, C.J.; Liu, J.J. Synthesis, structure and exchange bias in Cr₂O₃/CrO₂/Cr₂O₅ particles. *Thin Solid Film.* **2011**, *519*, 8423–8425. [[CrossRef](#)]
60. Singh, G.P.; Ram, S.; Eckert, J.; Fecht, H.J. Synthesis and morphological stability in CrO₂ single crystals of a half-metallic ferromagnetic compound. *J. Phys. Conf. Ser.* **2009**, *144*, 012110. [[CrossRef](#)]
61. Cheng, M.; Lu, Z.; Zhang, Z.; Yu, Z.; Liu, S.; Chen, C.; Li, Y.; Liu, Y.; Shi, J.; Xiong, R. Manipulation of film quality and magnetic properties of CrO₂ (100) films on TiO₂ substrates with carrier gas and growth temperature. *RSC Adv.* **2018**, *8*, 1562–1568. [[CrossRef](#)]
62. Sousa, P.M.; Dias, S.A.; Conde, O.; Silvestre, A.J.; Branford, W.R.; Morris, B.; Yates, K.A.; Cohen, L.F. Influence of Growth Temperature and Carrier Flux on the Structure and Transport Properties of Highly Oriented CrO₂ on Al₂O₃ (0001). *Chem. Vapor Depos.* **2007**, *13*, 537–545. [[CrossRef](#)]
63. Solecka, M.; Kusinski, J.; Kopia, A.; Rozmus-Górnikowska, M.; Radziszewska, A. High-Temperature Corrosion of Ni-Base Alloys by Waste Incineration Ashes. *Acta. Phys. Pol. A* **2016**, *130*, 1045–1048. [[CrossRef](#)]
64. Luo, M.; Ortiz, A.L.; Guo, F.; Shi, Z.; Li, L.; Ren, Y.; Zhang, X.; Chen, Z.; Shaw, L.L.; Chen, W. Mechanical activation enhanced solid-state synthesis of NaCrO₂ cathode material. *Materialia* **2019**, *5*, 100172. [[CrossRef](#)]
65. Fryburg, G.C.; Miller, R.A.; Kohl, F.J.; Stearns, C.A. Volatile Products in the Corrosion of Cr, Mo, Ti, and Four Superalloys Exposed to O₂ Containing H₂O and Gaseous NaCl. *J. Electrochem. Soc.* **1977**, *124*, 1738–1743. [[CrossRef](#)]
66. Opila, E.J.; Myers, D.J.; Jacobson, N.S.; Nielsen, I.M.B.; Johnson, D.F.; Olminky, J.K.; Allendorf, M.D. Theoretical and Experimental Investigation of the Thermochemistry of CrO₂(OH)₂(g). *J. Phys. Chem. A* **2007**, *111*, 1971–1980. [[CrossRef](#)] [[PubMed](#)]
67. Huang, W.; Huang, T.; Song, P.; Chen, R.; Zheng, B.; Wang, C.; Li, C.; Lu, J. CrO₂(OH)₂ volatilization rate and oxidation behavior prediction of the NiCr coating in air-H₂O environment at 650 °C. *Corros. Sci.* **2021**, *182*, 109303. [[CrossRef](#)]
68. Bunting, E.N. Phase equilibria in the system Cr₂O₃-Al₂O₃. *Bur. Stand. J. Res.* **1931**, *6*, 948. [[CrossRef](#)]
69. Zhao, P.; Zhao, H.; Yu, J.; Zhang, H.; Gao, H.; Chen, Q. Crystal structure and properties of Al₂O₃-Cr₂O₃ solid solutions with different Cr₂O₃ contents. *Ceram. Int.* **2018**, *44*, 1356–1361. [[CrossRef](#)]

Disclaimer/Publisher’s Note: The statements, opinions and data contained in all publications are solely those of the individual author(s) and contributor(s) and not of MDPI and/or the editor(s). MDPI and/or the editor(s) disclaim responsibility for any injury to people or property resulting from any ideas, methods, instructions or products referred to in the content.